Quantum Electronics **46** (11) 1015–1022 (2016)

INTERACTION OF LASER RADIATION WITH MATTER DOI: 10.1070/QEL16198

Surface, structural and mechanical properties of zirconium ablated by KrF excimer laser radiation

Nisar Ali, Shazia Bashir, Umm-i-Kalsoom, Narjis Begum, Syed Waqas Ahmad

Abstract. **We study the effect of the ambient – dry (air) and wet (propanol) – environment on the surface, structural and mechanical properties of zirconium samples after irradiation with a KrF excimer laser (wavelength of 248 nm, pulse duration of 20 ns and repetition rate of 20 Hz). The samples are exposed to an increasing number of laser pulses varying from 500 to 2000 in both media. Various features of the treated targets such as surface morphology, chemical composition, crystalline structure and hardness are analysed by complementary characterisation techniques, such as scanning electron microscopy (SEM), energy dispersive X-ray spectroscopy (EDS), X-ray diffraction (XRD), Raman spectroscopy and Vickers hardness tester, respectively. Surface morphology and hardness are explained on the basis of modifications in crystalinity, residual pressures and chemical properties of the sample surface after its irradiation.**

Keywords: *zirconium, laser ablation, ambient environment, surface morphology, crystalinity, hardness.*

1. Introduction

The interaction of nanosecond laser radiation with solid materials, accompanied by a variety of nonstationary effects, may results in the formation of various surface features. Surface modification is an effective technique for improving diverse surface characteristics of materials such as roughness, wear and corrosion resistance, hardness, etc. [1–3]. Laser ablation of solids in a liquid-confined environment has become an important method for the fabrication of debris-free microstructures on the surface of materials. The presence of a dense medium adjoining to the molten layer of the target causes various instabilities. In particular, various kinds of structures can be grown due to the viscous flow of the vapours of the surrounding liquid and its chemical reaction with metals. The spatial configuration of the structures produced under laser ablation of a solid confined into liquid depends on various experimental parameters, such as the laser spot size, fluence, number of laser pulses, properties of the surrounding liquid, etc. The chemical reactivity of most liquids with metals enhances the ablation efficiency without a momentous effect on the stoichiometry of the target [4, 5] and results in the formation of colloids and plasma-induced bubble cavitations due to the formation of oxides and metal alcohols. Particles and nanostructures produced by this technique show the interaction of dense vapours of liquids with the molten layer on the target surface. Hydrodynamic instabilities under such conditions are accountable for such interactions [6]. The molten layer behaves as a reservoir for the generation of nanoparticles and nanostructures. Laser ablation of metals in liquid confined environments has been the focus of interest of many researchers. Recently, Barmina et al. [7] has reported that the growth of nanostructures on the tungsten surface after ablation in a liquid environment has improved its thermionic properties. Laser ablation in the liquid confined environment involves heat transfer (as a result of convection and/or conduction) and bubble motion, which contributes to the removal of redeposited particles from the surface and reduces the debris oxidation [8]; as a result, the increased energy coupling to the target is directed to clean the target surface and make it hygienic [9, 10].

The aim of the present work is to investigate the effect of the ambient environment and the number of laser pulses on the surface morphology, grains growth behaviour, chemical composition, crystallinity and hardness of a zirconium target after laser ablation. The growth of various structures and variations in hardness can be well correlated with the changes produced in the crystallinity due to enhancement of chemical reactivity of zirconium. For this purpose, zirconium targets are ablated with an increasing number of KrF excimer laser pulses in air and propanol environments. Various diagnostic techniques, such as scanning electron microscopy (SEM), energy dispersive X-ray spectroscopy (EDS), X-ray diffractometery (XRD), Raman spectroscopy and Vickers microhardness and CSM nanohardness techniques, are employed to correlate the surface features with the change in the chemical composition and crystallinity after irradiation.

2. Experimental setup

A KrF excimer laser (EX 200/125-157 GAM Laser, the USA) with a centre wavelength of 248 nm, pulse duration of 20 ns,

Nisar Ali Department of Basic Sciences and Humanities, University of Engineering and Technology Lahore, Faisalabad Campus, Faisalabad, Pakistan; Centre for Advanced Studies in Physics, GC University 1-Chruch Road Lahore, Pakistan; Department of Physics, GC University Kachehry Road Lahore, Pakistan; e-mail: chnisarali@gmail.com;
Shazia Bashir Centre for Advanced Studies in Physics, GC University 1-Chruch Road Lahore, Pakistan;
Umm-i-Kalsoom Department of Physics, Riphah International University Islamabad (Lahore Campus) Lahore, Pakistan;
Narjis Begum Department of Physics, COMSATS Institute of Information Technology, Islamabad, Pakistan;
Syed Waqas Ahmad Department of Chemical Engineering, University of Engineering and Technology Lahore, Faisalabad Campus, Faisalabad, Pakistan

Received 14 August 2016; revision received 9 September 2016
Kvantovaya Elektronika **46** (11) 1015–1022 (2016)
Submitted in English

repetition rate of 20 Hz and pulse energy of 70 mJ was employed for ablation of a zirconium target. The laser beam was focused on the target surface by using a lens with a focal length of 50 cm.

The rectangular-shaped zirconium targets measuring $8 \times 8 \times 2$ mm were grinded, polished and ultrasonically cleaned with acetone for 30 min. The prepared targets were placed in a quartz cuvette of size $10 \times 10 \times 45$ mm. The schematic of the experimental setup is shown elsewhere [10]. Irradiation was carried out 5 cm in front of the focus position, for a fixed laser fluence of 3.6 J cm^{-2}. Zirconium targets were exposed for a various number of overlapping laser pulses, i.e. 500, 1000, 1500 and 2000. Under the same laser parameters, two sets of experiments were performed, i.e. in air and propanol. In the case of propanol, for each exposure the quartz cuvette was filled with fresh liquid whose thickness over the sample was about 4 mm.

At a wavelength of 248 nm, the percentage laser energy absorption was calculated to be 6% for propanol. The value of the absorption coefficient α was evaluated for propanol by using the Beer–Lambert law and amounted to 1.5×10^{-2} mm^{-1}.

The surface morphology of ablated targets was investigated using a SEM-JEOL JSM-6480 LV scanning electron microscope. An EDS-S3700N energy dispersive X-ray spectroscope was used for chemical analysis. An X'Pert PRO (MPD) X-Ray diffractometer was employed to determine the crystallographic structure and phase analysis. Raman spectroscopy was carried out to determine structural modifications of the irradiated zirconium. Micro- and nanohardness were measured using a HV-1000A Vickers microhardness tester and a CSM instruments (NHT+MHT) nanohardness tester, respectively.

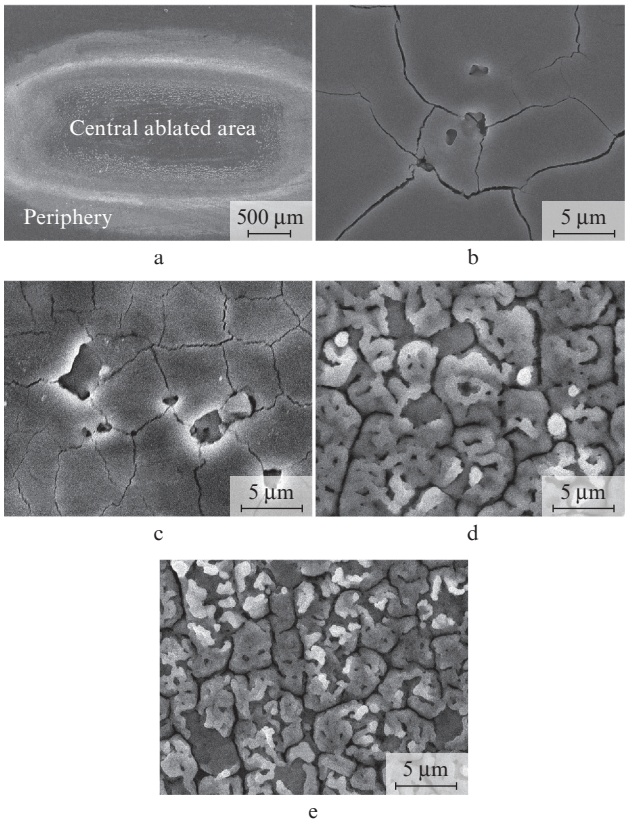

Figure 1. SEM images of (a) overall view of the ablated crater after excimer laser irradiation with 500 laser pulses at a fluence of 3.6 J cm^{-2} and (b–e) magnified SEM images of the central ablated area revealing the variation in the surface morphology of zirconium ablated in air by (b) 500, (c) 1000, (d) 1500 and (e) 2000 laser pulses.

3. Results and discussion

Figure 1a shows a significantly modified surface morphology after irradiation with 500 overlapping laser pulses at a fluence of 3.6 J cm^{-2} in air. An overall view of the ablated area shows the appearance of a rectangular-shaped crater along with the redeposited material at the periphery after irradiation. When a very small surface area of the target is irradiated by intense laser pulses, a tremendously high-pressure and high-temperature region is formed and a high-density ablation plume is created which expands into the ambient air. Further expansion of the plume front compresses the ambient air and rapidly decelerates developing a strong external shock wave which propagates in a radially outward direction. Initially highly heated and low density background region behind the strong expanding shock front flows back into the inner region. When the shock-wave intensity weakens, the inner gas cools by conduction and radiation. This inward flow efficiently drags and redeposits the debris particles of the plume onto the target surface [11].

Figures 1b–1e show SEM images of the central ablated area of zirconium in air for a various number of pulses. In Fig. 1b one can see large grains with cavities along the grain boundaries. Laser-induced heating and cooling, incredible temperature gradient, laser-induced residual stresses and diffusion of oxygen along the grain boundaries are responsible for this kind of grain growth [12, 13]. When the laser pulse terminates, the molten material generated by fast heating is supercooled and acts as an effective heat sink that quickly removes any released latent heat and causes the crystal growth. Atoms at the grain boundary are loosely packed, and have higher values of energy as compared to the atoms in the lattice. The net number of atoms at the grain boundary reduces, as the grains grow in size and their numbers decrease, and thereby the free energy of the system reduces.

An atom performs a tedious thermal motion at the grain boundary. Most of the time, this atom oscillates with small magnitude. Sometimes, the atom jumps from the boundary of one atom and get attached to the lattice of the other grain. The probability of jumping of electrons in forward and backward directions will be the same if the two states have an identical energy but the probability will be biased if the two states have different energies. This bias results in macroscopic migration of the grain boundary, in the direction that reduces the energy of the system and causes grain growth.

Cavities are formed by the liberation of adsorbed gases beneath the surface during laser irradiation, due to volume boiling [14]. Figure 1c exhibits the significantly reduced grain size with increasing density. A decrease in the grain size with increasing number of pulses is due to the enhanced interstitial diffusion of oxygen into the surface during recrystallisation process (confirmed by EDS and XRD results). Refilling of cavities by a melted and shock liquefied material causes reduction in the size of cavities [15]. A further increase in the number of laser pulses up to 1500 (Fig. 1d) results in large agglomerates with enhanced density of cavities. The surface material also appears to be detached from the surface. An explosive melt expulsion can cause this kind of structure [16]. For 2000 laser pulses (Fig. 1e), a redeposited material in the form of flakes is

observed over the surface. Large diffused grains with wider grain boundaries are also seen in background.

Figure 2 presents the surface morphology of the zirconium sample after irradiation with a various number of overlapping laser pulses at 3.6 J cm^{-2} in propanol. Figure 2a shows the surface morphology of the zirconium sample after irradiation with 500 laser pulses. A significant difference in the crater appearance is observed under dry and wet ablation. Contrary to ablation in air, no significant resolidification of the material around the edges of the craters is observed because the ablated species are taken away by the surrounding liquid [17]. The liquid has played a considerable role in ablation of zirconium and it effectively cools the target, preventing the unnecessary heat accumulation after laser irradiation.

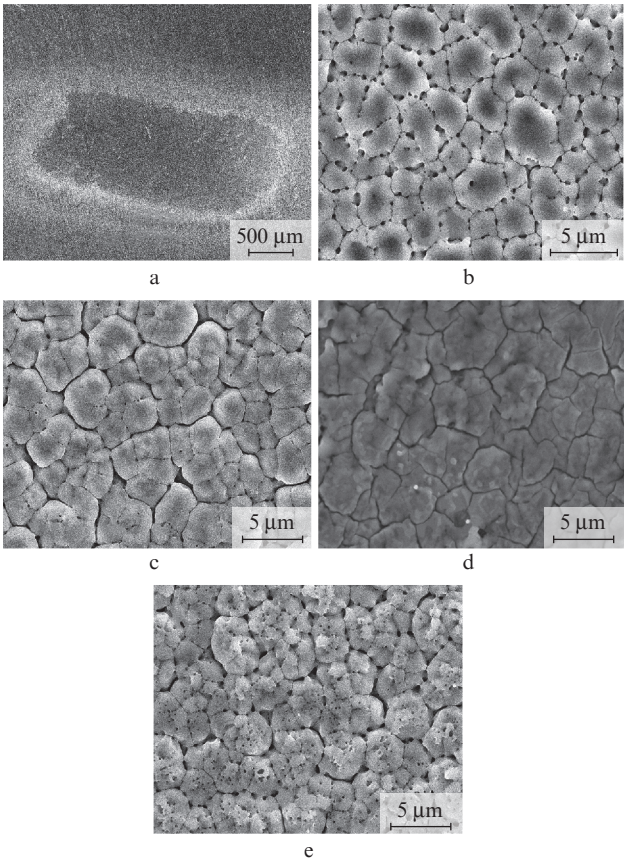

Figure 2. Same as in Fig. 1, but for ablation of zirconium in propanol.

Figures 2b–2e present enlarged SEM images of the morphology of the central ablated area of zirconium in propanol for a various number of overlapping laser pulses. Figure 2b shows the development of grains with distinct grain boundaries for 500 pulses. The high density of cavities is also seen across the grain boundaries. Volume boiling during irradiation may cause the formation of cavities due to the release of gases underneath the surface [18]. With increasing number of pulses up to 1000, breaking of large grains into smaller ones results in a significantly enhanced density and a reduced size alongside with diffused grain boundaries (Fig. 2c). This is due to transformation of the pores and cavities into a greater number of small grains under multipulse irradiation [10]. With a further increase in the number of laser pulses up to 1500, the grain size increases with increasing compactness of the surface (Fig. 2d). With 2000 laser pulses, a significantly modified surface morphology with reduction in grain size and porous microstructure is observed. Grain boundaries become wider with cavities across the grain boundaries and a large number of pores within the grains are observed (Fig. 2e). The bubble nucleation sites instigated by boiling of the molten liquid cause the formation of pores and cavities [16]. Laser-induced heating and melting of the zirconium target stimulates reaction between the molten surface and oxygen/hydrogen/carbon (confirmed by XRD and Raman analysis). During the recrystallization process at solid-liquid interface oxygen/hydrogen/carbon diffused into the target surface causes wider and distinct grain boundaries [13].

Comparison of the results of ablation in both, air (Fig. 1) and propanol (Fig. 2), media shows significant dissimilarities in the surface morphology of ablated zirconium. In the case of air, maximum ablation occurs in the central ablated area while in the case of propanol, it is more uniformly distributed. As Kim et al. [19] suggested, the shock-wave propagation and the recoil momentum presented by the vapour plume expulsion cause the surface depression in the central ablated area and generate the shoulder at the periphery. On the contrary, in the liquid, the removal is more uniform without the appearance of a shoulder at the periphery of the ablated area. A rapid temperature rise during laser-induced plasma expansion generates bubbles in the liquid. The bubble motion is responsible for the removal of ablated particles [20]. Large, well-defined grains are observed in case of dry ablation with distinct grain boundaries for a smaller number of laser pulses.

Laser-induced melting of the target produces excess vacancies, which causes increased diffusion across the grain boundaries and gives rise to the tensile stresses and grain growth. With increasing number of pulses, melting of the material is observed with a porous microstructure and flakes over the surface representing the exfoliational sputtering, whereas, in case of wet ablation, distinct, well-defined and small grains with a high density of cavities and pores over the surface are developed. During irradiation of zirconium in the liquid, a plasma plume from the solid target will be generated at the solid–liquid interface, which remains confined [21, 22]. A shock wave is produced in the plasma plume by the laser-induced plasma due to the confinement of the liquid. This shock wave will induce an extra pressure in the laser-induced plasma, called plasma-induced pressure [22]. The plasma-induced pressure will lead to an additional temperature rise of the laser-induced plasma. Therefore, the shock wave generated by the expansion of the laser-induced plasma under the confinement of the liquid pushes the laser-induced plasma into a thermodynamic state of the higher temperature, higher pressure and higher density [21, 22]. Under this confinement effect, the pronounced heat accumulation takes place which enhances the density of grains on the irradiated surface.

The chemical analysis of unirradiated and irradiated zirconium targets is performed using EDS. Table 1 shows the results of the comparative EDS analysis for the unirradiated sample and the central ablated area of the zirconium target after its irradiation with 1000 excimer laser pulses in ambient environments of air and propanol. The cavities observed in the case of ablation in air (dry ablation) (Fig. 1) can be attributable to the reduction of carbon and complete removal of boron and rhenium [23]. A maximum increase in the oxygen content from 4.91% to 23.86% is observed for ablation in air, whereas in propanol its value is 17.03%. An increase in the content of car-

Table 1. Results of the EDS analysis of the unirradiated zirconium target and its central part irradiated by 1000 excimer laser pulses in the air and propanol at a fluence of 3.6 J cm^{-2}, wavelength of 248 nm, pulse duration of 20 ns and pulse repetition rate of 20 Hz.

Elements	Content in the sample/wt %		
	Unirradiated	Irradiated in air	Irradiated in propanol
Zirconium	87.52	74.22	75.02
Boron	2.78	–	2.02
Carbon	2.82	1.92	4.51
Oxygen	4.91	23.86	17.03
Rhenium	1.97	–	1.42

bon from 2.82% to 4.51% is also observed under ablation in propanol. Multipulse irradiation induced heating of zirconium causes efficient diffusion of atomic oxygen into the target surface, and therefore oxides are formed [13].

We used the X-ray diffraction technique to identify variations in cryastallinity and residual stresses. Figure 3 shows XRD patterns of an unirradiated zirconium target with peaks of (100), (002), (101), (102), (110), (103), (004) and (104) crystalline planes.

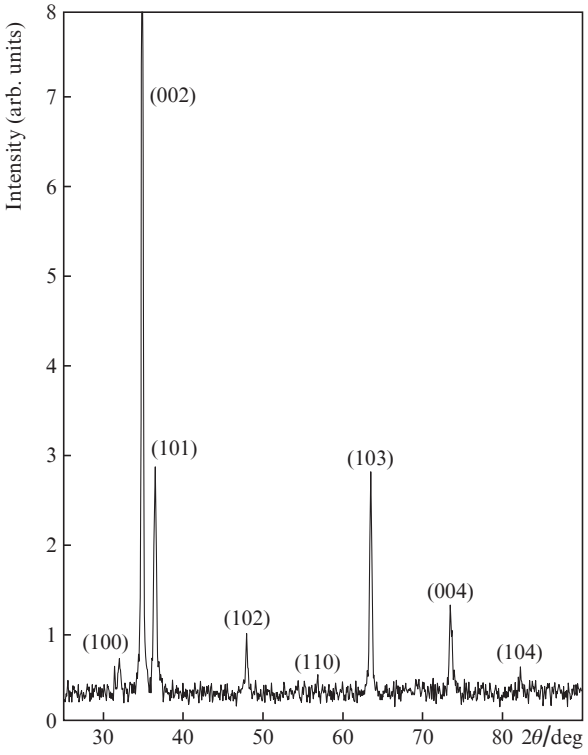

Figure 3. XRD patterns of unirradiated zirconium.

Figure 4 presents XRD diffractograms of laser ablated zirconium samples for a different number of overlapping laser pulses in air. New phases of zirconium oxides, i.e. ZrO_2 [(111), (212), (321)], Zr_3O [(201), (200), (232)] and Zr_2O (322), are observed along with the original phases of zirconium. The crystallite size D is evaluated for ZrO_2 (212) plane reflection by using Sherrer's formula [24]

$$D = \frac{0.9\lambda}{\Delta \cos\theta}, \tag{1}$$

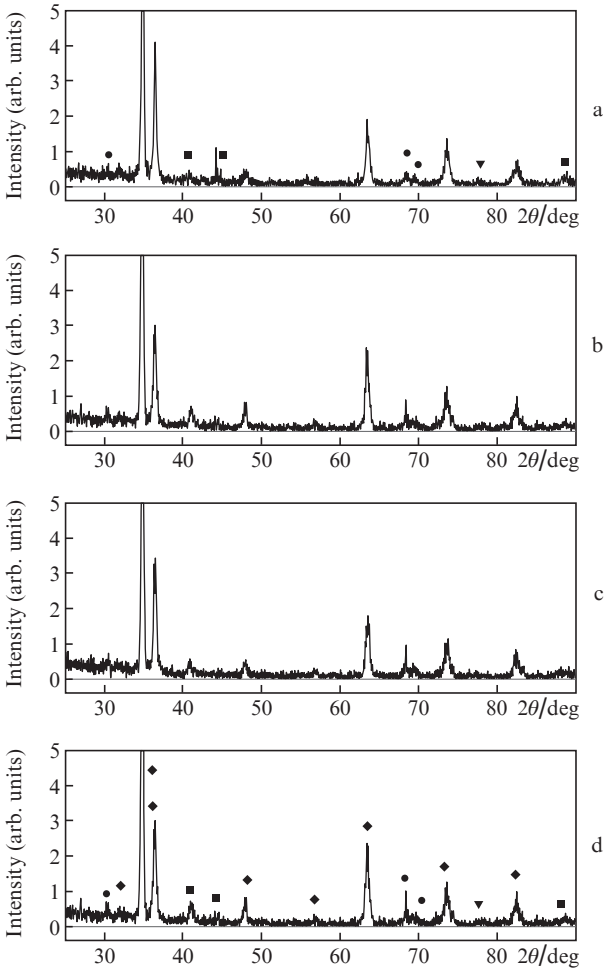

Figure 4. XRD patterns of zirconium samples irradiated in air by (a) 500, (b) 1000, (c) 1500 and (d) 2000 excimer laser pulses. Points show the reflection peaks of (♦) Zr, (●) ZrO_2, (▼) Zr_2O and (■) Zr_3O.

where λ is the wavelength of X-rays (1.5406 Å), Δ is the FWHM of the reflectance peak and θ is the angle of diffraction. The residual strains ε are evaluated by the relation [24, 25]

$$\varepsilon = \frac{d - d_0}{d_0}, \tag{2}$$

where d is the observed and d_0 is the standard spacing between the crystalline planes. The induced stresses σ are defined as

$$\sigma = \varepsilon E, \tag{3}$$

where E is the Young modulus, equal to 186.21 GPa for ZrO_2 [26].

Both the peak intensity (Fig. 4) and crystallite size (Fig. 5) are found to increase with increasing number of laser pulses. This is due to increased diffusion of oxygen into the surface across the grain boundaries [13] and enhancement of diffraction of X-rays from the target surface [25]. The diffusion of oxygen in zirconium after irradiation is also exhibited in the EDS analysis (Table 1). The interaction of laser radiation with the zirconium surface changes its microstructure and Bragg's conditions of diffraction. These variations are attributable for the changes in d spacing and intensity of diffraction lines [13].

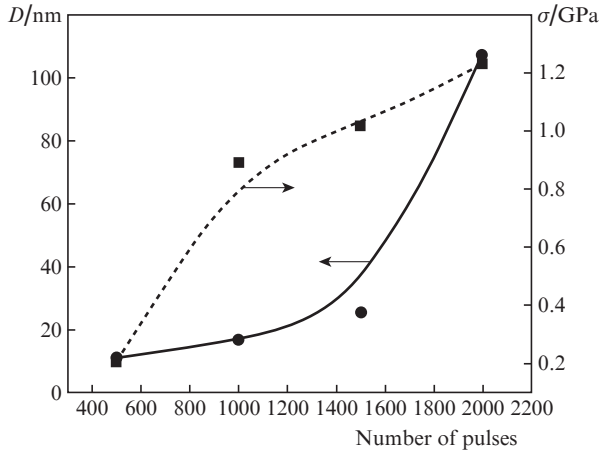

Figure 5. Dependences of the crystallite size D and residual stresses σ of laser irradiated zirconium on the number of overlapping laser pulses in air.

The dependence of residual stresses on the number of pulses is also shown in Fig. 5. Laser-induced thermal shocks and lattice defects generated by incorporation of oxygen ions into the lattice may cause residual stress variation. Compressive stresses are generally due to ion implantation, whereas laser-induced thermal shocks are responsible for tensile stresses [27]. For 500 accumulated laser pulses, less pronounced tensile residual stresses are present, which afterwards increase with increasing number of laser pulses up to 2000. Thermally induced shocks lead to an increase in tensile stresses and crystal growth. The enhanced effects of thermal shocks and stresses cause the formation of pronounced cavities and pores which are observed in Figs 1b–1e [18, 25].

Figure 6 presents the XRD diffractograms of laser ablated zirconium samples for a different number of overlapping laser pulses in propanol. New phases of zirconium oxides [ZrO_2 (212), (114) and Zr_3O (201)] and hydride [ZrH_2 (112)] are observed along with the original phases of zirconium. The peak intensity of the ZrO_2 (212) plane reflection increases with increasing number of laser pulses up to 2000 (Fig. 6).

Figure 7 shows variations in both crystallite size and stresses induced after irradiation. The crystallite size decreases with increasing number of laser pulses up to 1500. With increasing number of laser pulses up to 2000, the crystallite size increases. After ablation by 500 laser pulses, highly tensile stresses are present which relax with increasing number of laser pulses up to 1500. A further increase in laser pulses causes an increase in tensile stresses. These results are also well correlated with the change in the surface morphology [Figs 2b–2e]. After ablation by 500 laser pulses (Fig. 2b), the presence of cavities is evident for the presence of highly tensile residual stresses. With increasing number of pulses up to 1500, a reduction in density of cavities and pores is observed corresponding to relaxation in tensile residual stresses (Figs 2b–2d). With increasing number of laser pulses up to 2000, the high density of pores and cavities confirms the increase in tensile stresses again (Fig. 2e).

Comparison of the XRD data of dry (air, Figs 4, 5) and wet (propanol, Figs 6, 7) media shows significant dissimilarities in the chemical composition. In the case of ablation in air, only oxides are formed, while in the case of ablation in propanol, oxides are formed along with hydrides. For both media variations in the peak intensity, crystallinity and residual stresses are observed.

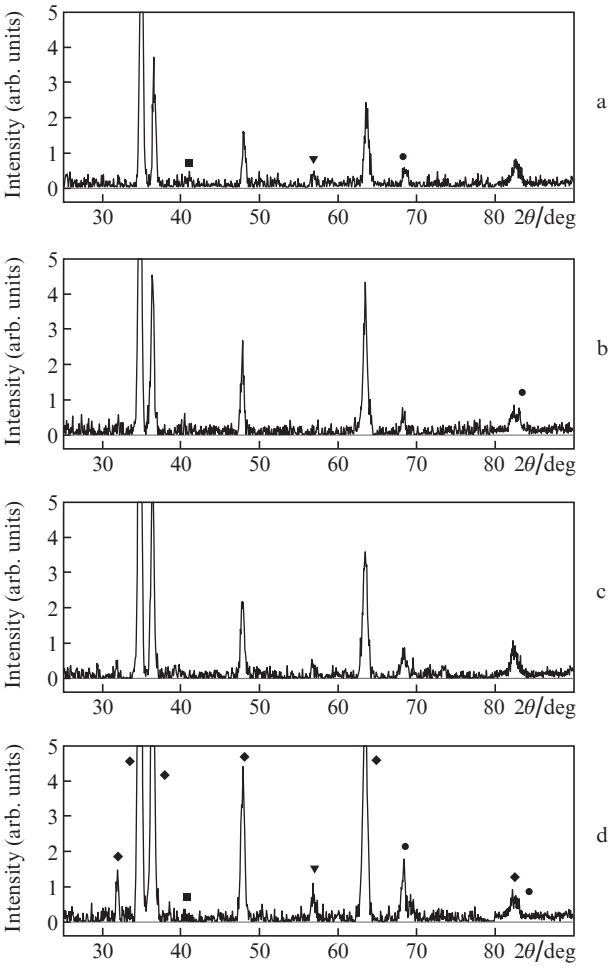

Figure 6. XRD patterns of zirconium samples irradiated in propanol by (a) 500, (b) 1000, (c) 1500 and (d) 2000 excimer laser pulses. Points show the reflection peaks of (♦) Zr, (●) ZrO_2, (■) Zr_3O and (▼) ZrH_2.

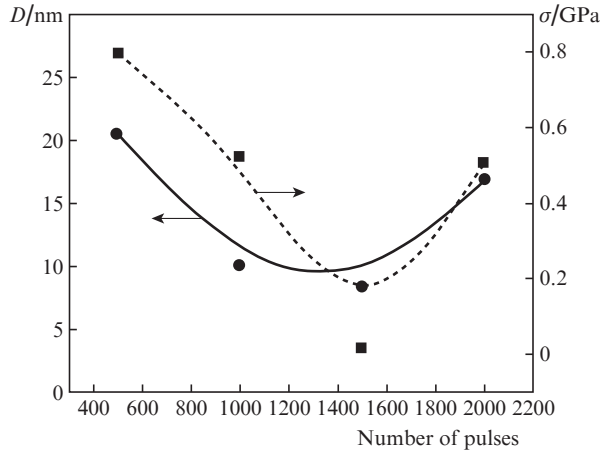

Figure 7. Dependences of the crystallite size D and residual stresses σ of laser irradiated zirconium on the number of overlapping laser pulses in propanol.

Figure 8 shows the Raman spectra of zirconium samples irradiated by a various number of laser pulses at a fluence of 3.6 J cm^{-2} in air and propanol. Raman modes arise from laser-induced ablation of zirconium and formation of oxides on the metal surface.

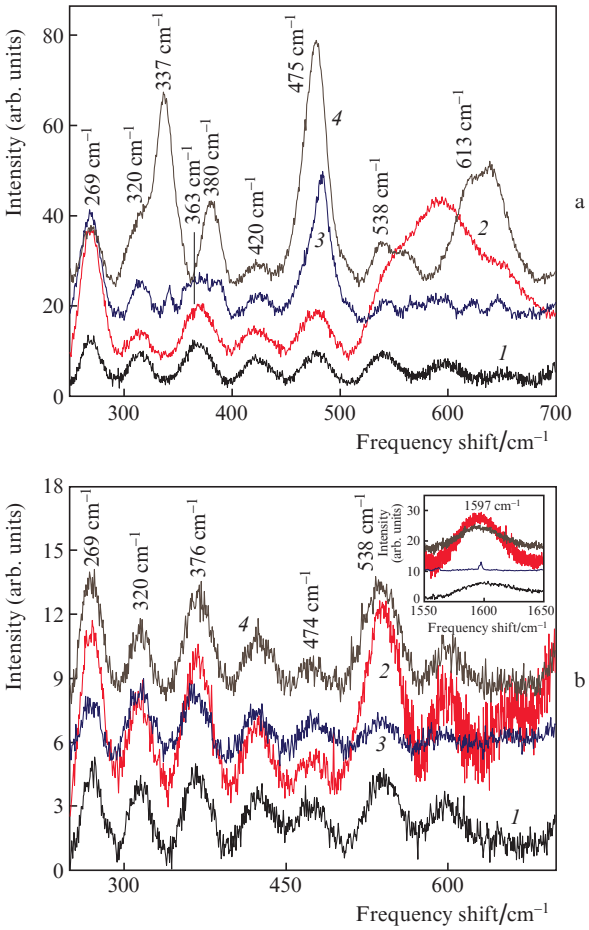

Figure 8. Raman spectroscopy analysis of zirconium irradiated in (a) the air and (b) propanol by an excimer laser with (*1*) 500, (*2*) 1000, (*3*) 1500 and (*4*) 2000 pulses.

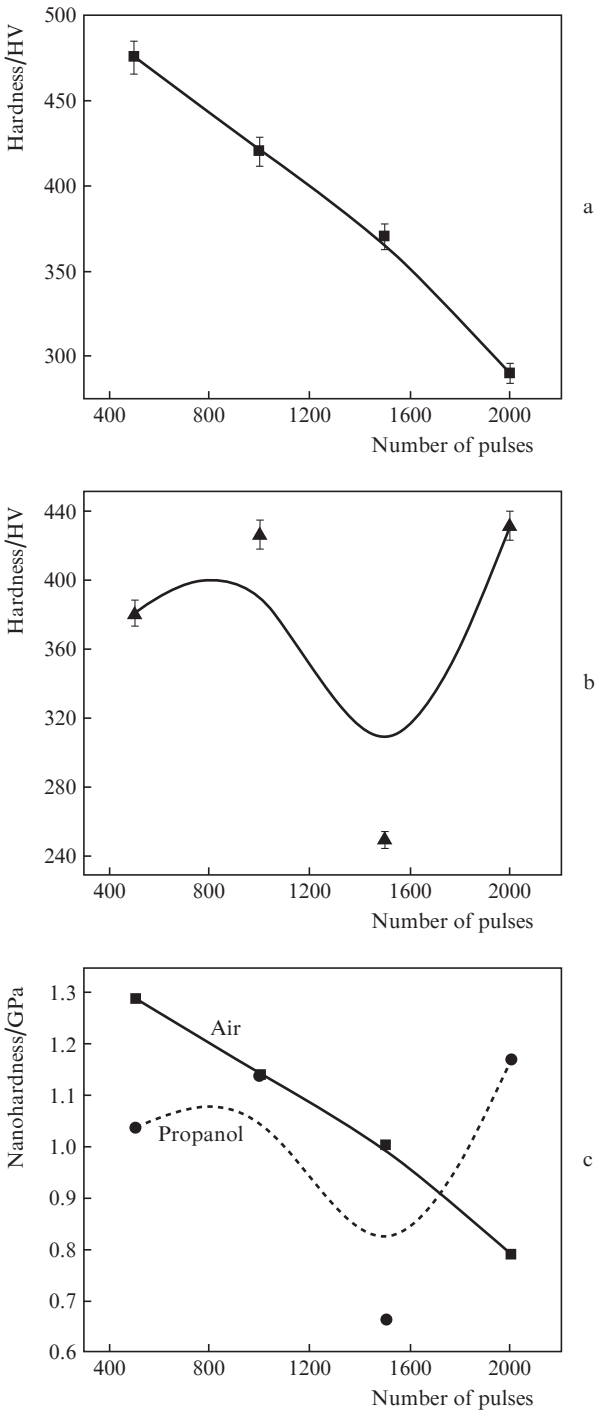

Figure 9. Microhardness of zirconium ablated by an excimer laser in (a) the air and (b) propanol, as well as (c) nanohardness of zirconium ablated by an excimer laser in both media as functions of the number of pulses.

In the case of ablation in air (Fig. 8a), the Raman peaks at 320 and 337 cm^{-1} correspond to the Zr–Zr bond, while peaks at 475, 538 and 613 cm^{-1} confirm the presence of the O–O bond [28]. Peaks observed at 363, 380 and 420 cm^{-1} are the characteristic bands of monoclinic ZrO_2 [28–31], and the Raman peak at 269 cm^{-1} can be assigned to the presence of tetragonal ZrO_2 [32]. With increasing number of laser pulses, the intensity of almost all bands increases which indicates the formation of more oxides on the surface due to enhanced oxygen diffusion (also evident from EDS and XRD analysis) [33].

In the case of ablation in propanol (Fig. 8b), the Raman peak at 320 cm^{-1} corresponds to the Zr–Zr bond, whereas peaks at 474 and 538 cm^{-1} confirm the presence of the O–O bond [28]. A peak at 376 cm^{-1} is the characteristic band of monoclinic ZrO_2 [29–31] and the peak at 269 cm^{-1} can be assigned to the presence of tetragonal ZrO_2 [32]. The inset of Fig. 8b also shows the presence of zirconium hydride (ZrH) at 1597 cm^{-1}. Thus, the results of Raman spectroscopy are in good agreement with the EDS and XRD results.

The untreated zirconium sample has a hardness value of 266 HV. Figure 9 shows the variation in hardness of zirconium targets irradiated by nanosecond laser pulses in air and propanol as a function of the number of laser pulses. After ablation by 500 laser pulses in air (Fig. 9a), the hardness value of 475 HV is observed, which is 1.78 times greater than the hardness of the unirradiated target. An increase in the number of laser pulses up to 2000 shows a continuous decrease in the hardness up to 290 HV, which is 1.09 times of the hardness of the untreated target.

After ablation by 500 laser pulses in propanol (Fig. 9b), the hardness value of 380 HV is observed, which is 1.42 times greater than the hardness of the unirradiated target. With increasing number of laser pulses up to 1000, hardness increases up to 420 HV, which is 1.57 times greater than the hardness of the unirradiated target. A further increase in the number of laser pulses up to 1500 shows a decrease in hardness down to 245 HV, which is 0.92 times of the hardness of

the unirradiated target. With 2000 laser pulses, the hardness value of 430 HV is observed, which is 1.61 times of the hardness of the unirradiated target.

Figure 9c shows the dependences of nanohardness of zirconium irradiated both in dry and wet media on the number of pulses.

A decrease in hardness of the irradiated targets can be explained on the basis of an increasing crystallite size and enhanced tensile residual stresses. Oxygen diffusion across the grain boundaries results in larger crystallites (Fig. 5) that are more prone to coarsening, leading to a lower crystallite density and a lower hardness [34–36]. An increase in hardness is attributable to interstitial diffusion of oxygen into the lattice, which results in a decrease in the crystallite size and tensile residual stresses (Fig. 7) [34, 37]. A smaller crystallite size is efficient in obstructing the dislocation movement and is responsible for the high strength and hardness. Despite the smaller crystallite size, a lower value of hardness was observed by Mayrhofer et al. [37, 38]. The authors showed that the Hall–Petch relationship between hardness and grain size breaks down for very small values of the crystallite size with limited dislocation plasticity. The critical crystallite size reported by Mayrhofer et al. was 12 nm. In our case, after ablation by 1500 laser pulses in propanol, the observed crystallite size is ~8 nm. This is the reason for softening of material after irradiation with 1500 laser pulses. These results can be verified by using the Hall–Petch relationship [39]:

$$H = H_0 + K_H a^{-1/2},$$

where H_0 and K_H are the experimental constants, a is the average grain size and H is the hardness. Variations in hardness depend on some factors, including lattice defects, density of oxide contents, phase composition, grain size distribution, crystal structure, etc. [40].

4. Conclusions

Surface, structural and mechanical properties of zirconium samples after irradiation with a KrF excimer laser for a various number of pulses in dry (air) and wet (propanol) media have been investigated. Both dry and wet media play a significant role in structural, chemical and mechanical modifications of the irradiated zirconium surface. The presence of liquids helps in removing the ablation debris and reducing the thermal damages, as well as provides cleaner ablation of zirconium than those air-mediated mechanisms. As a result, the surface morphologies of the craters produced in liquids are much smoother. Additionally, the surfaces of the craters formed in propanol are smoother than those produced in air, which might be due to the different interacting mechanisms, such as recoil pressures, production of bubbles, and laser-induced surface melting of zirconium. Granular morphology with large, well-defined grains is observed in the case of dry ablation. In the case of wet ablation, the material again shows a granular morphology but the size of these grains is much less than those produced in the case of dry ablation. The EDS analysis confirms an increase in the content of oxygen in air and a simultaneous increase in the content of oxygen and carbon in propanol. The XRD analysis confirms the diffusion of oxygen in the case of dry ablation of zirconium, which is responsible for the formation of oxides on its surface. In the case of wet ablation, the diffusion of oxygen and hydrogen causes the formation of oxides and hydrides on the metal surface. The Raman analysis supports the EDS and XRD results and confirms the formation of oxides during dry ablation and the formation of both oxides and hydrides during wet ablation. Hardness decreases with increasing number of laser pulses in the case of dry ablation, whereas, in the case of wet ablation in propanol, it first decrease and then increase with increasing number of laser pulses. Variations in hardness depend on a number of factors including the lattice defects, density of oxide contents, phase composition, grain size and distribution and crystal structure.

Acknowledgements. The authors thank the Higher Education Commission of Pakistan (HEC) for providing sufficient funds for the project 'Upgrade of laser lab facilities at CASP, GC University Lahore Pakistan' and for providing financial support (Indeginois Scholarship) to the first and third authors.

We also like to thank the Chairman of the Physics Department at the UET (Lahore, Pakistan) for providing the Raman facility and the Director at CASP, GC University (Lahore, Pakistan) for providing SEM and XRD facilities.

References

1. Shafeev G.A., Obraztsova E.D., Pimenov S.M. *Appl. Phys. A*, **65**, 29 (1997).
2. Simakin A.V., Voronov V.V., Kirichenko N.A., Shafeev G.A. *Appl. Phys. A*, **79**, 1127 (2004).
3. Barmina E.B., Stratakis E., Fotakis C., Shafeev G.A. *Kvantovaya Elektron.*, **40**, 1012 (2010) [*Quantum Electron.*, **40**, 1012 (2010)].
4. Kazakevich P.V., Simakin A.V., Shafeev G.A. *Appl. Surf. Sci.*, **252**, 4457 (2006).
5. Masahiro K.A., Nakanoc H., Hashidad M., Kattoe M., Abea N., Fujitaf M. *Vacuum*, **80**, 1346 (2006).
6. Landau L.D., Lifshits E.M. *Fluid Mechanics* (Oxford: Pergamon, Elmsford, 1987).
7. Barmina E.V., Stratakis E., Barberoglou M., Stolyarove V.N., Stolyarove I.N., Fotakis C., Shafeev G.A. *Appl. Surf. Sci.*, **258**, 5898 (2012).
8. Ren M.K.J., Heeselink L. *Opt. Lett.*, **30**, 1740 (2005).
9. Bashir S., Vaheed H., Mahmood K. *Appl. Phys. A*, **110**, 389 (2013).
10. Ali N., Bashir S., Umm-i-Kalsoom, Akram M., Mahmood K. *Appl. Surf. Sci.*, **270**, 49 (2013).
11. Singh M.A.S., Tsui Y.Y., Fedosejevs R. *J. Appl. Phys.*, **98**, 113520 (2005).
12. Tarasenko V.F., Goncharenko I.M., Koval N.N., Orlovskii V.M., Fedenev A.V., Velikanov S.D., Borisov V.P., Podavalov A.M., Zolotov M.I., Podsezertsev A.L., Tkachev A.N., Yakovlenko S.I. *Laser Phys.*, **13**, 1478 (2003).
13. Mahmood K., Farid N., Ghauri I.M., Afzal N., Idrees Y., Mubarik F.E. *Phys. Scr.*, **82**, 045606 (2010).
14. Craciun V., Craciun D. *Phys. Rev. B*, **58**, 6787 (1998).
15. Douglas B.C., Graham K.H. *Pulsed Laser Deposition of Thin Films* (New York–Chichester–Brisbane–Toronto–Singapore: Wiley-Interscience Publication, 1994).
16. Karimzadeh R., Anvari J.Z., Mansour N. *Appl. Phys. A*, **94**, 949 (2009).
17. Amorusso S., Bruzzese R., Spinelli N., Velotta R. *J. Phys. B*, **32**, R131 (1999).
18. Barata A., Cunha L., Moura C. *Thin Solid Films*, **398-399**, 501 (2001).
19. Kim D., Ye M., Gregoropoulos C.P. *Appl. Phys. A*, **67**, 169 (1998).
20. Muravitskaya E.V., Rosantsev V.A., Belkov M.V., Ershov-Pavlov E.A., Klyachkovs E.V. *Spectrochim. Acta*, *Part B*, **64**, 119 (2009).
21. Sasaki K., Takada N. *Pure Appl. Chem.*, **82**, 1317 (2010).
22. Yang G.W. *Prog. Mater. Sci.*, **52**, 648 (2007).
23. Yilbas B.S., Khaled M., Karatas C., Uslan I., Keles O., Usta Y., Ahsan M. *Surf. Coat. Technol.*, **201**, 679 (2006).

24. Ashraf M., Akhtar S.M.J., Khan A.F., Ali Z., Qayyum A. *J. Alloys Compd.*, **509**, 2414 (2011).
25. Khan I.A., Hassan M., Ahmad R., Qayyum A., Murtaza G., Zakaullah M., Rawat R.S. *Thin Solid Films*, **516**, 8255 (2008).
26. Shackelford J.F., Alexander W. *CRC Materials Science and Engineering Handbook* (California, USA, CRC Press, 2000).
27. Gurarie V.N., Otsuka P.H., Jamieson D.N., Prawe S. *Nucl. Instrum. Methods Phys. Res. B*, **242**, 421 (2006).
28. Kim B.K., Hamaguchi H. *Phys. Status Solidi B*, **203**, 557 (1997).
29. Tan D., Lin G., Liu Y., Teng Y., Zhuang Y., Zhu B., Zhao Q., Qiu J. *J. Nanopart. Res.*, **13**, 1183 (2011).
30. Haines J., Leger J.M.J. *Am. Ceram. Soc.*, **80**, 1910 (1997).
31. You J.L., Chang J.G., Hua Y.S., Jin-Chang M.A., Kuang-Di X. *Chin. Phys. Lett.*, **18**, 991 (2001).
32. Li Z.F.M., Xiong G., Ying P., Xin Q., Li C. *J. Phys. Chem. B*, **105**, 8107 (2001).
33. Ferreira M.G.S., Silva T.M., Catarino A., Pankuch M., Melendres C.A. *J. Electrochem. Soc.*, **139**, 3146 (1992).
34. Kusaka K., Taniguchi D., Hanabusa T., Tominaga K. *Vacuum*, **59**, 806 (2000).
35. Umm-i-Kalsoom, Ahmad R., Ali N., Khan I.A., Saleem S., Ikhlaq U., Khan N. *Plasma Sci. Technol.*, **15**, 666 (2013).
36. Corengia P., Ybarra G., Moina C., Cabo A., Broitman E. *Surf. Coat. Technol.*, **200**, 2391 (2005).
37. Mayrhofer P.H., Tischler G., Mitterer C. *Surf. Coat. Technol.*, **142-144**, 78 (2001).
38. Mayrhofer P.H., Mitterer C., Musil J. *Surf. Coat. Technol.*, **174-175**, 725 (2003).
39. Lim Y.Y., Chaudhri M.M. *Philos. Mag. A*, **82**, 2071 (2002).
40. Warcholinski B., Gilewicz A. *J. Achiev. Mater. Manuf. Eng.*, **37**, 498 (2009).